Determination of the interface energies of spherical, cuboidal and octahedral face-centered cubic precipitates in Cu-Co, Cu-Co-Fe and Cu-Fe alloys

doi: 10.1016/j.actamat.2008.12.028

Determination of the interface energies of spherical, cuboidal and octahedral fcc precipitates in Cu-Co, Cu-Co-Fe and Cu-Fe alloys

Daizen Watanabe, Chihiro Watanabe and Ryoichi Monzen*

D. Watanabe and C. Watanabe

Division of Innovative Technology and Science, Kanazawa University, Kakuma-machi, Kanazawa 920-1192, Japan.

R. Monzen *Corresponding author

Division of Innovative Technology and Science, Kanazawa University, Kakuma-machi, Kanazawa 920-1192, Japan.

E-mail address: monzen@t.kanazawa-u.ac.jp

***Keywords**:* Coarsening theory; Interface energy; Co-Fe precipitate; Copper-Cobalt-Iron alloy

Abstract

The coarsening theory of a spherical particle in a ternary alloy developed by Kuehmann and Voorhees (KV) has been generalized to any centro-symmetric particle. A classical thermodynamic analysis reveals that the generalized KV theory enables us to estimate the interface energy of a particle with a fixed shape, even if the shape of the particle is not controlled by minimization of the interface energy. Data on the coarsening of spherical, {001}-faceted cuboidal and {111}-faceted octahedral precipitates in a Cu-Co alloy, a Cu-Fe alloy, and three Cu-Co-Fe alloys with different Co and Fe contents during aging at 873 to 973 K have been collected by transmission electron microscopy and electrical resistivity. By applying the generalized KV theory to the experimental data, the energies of sphere, {001} and {111} interfaces have been determined. Their energies increase with increasing the Fe composition in the alloys.

1. Introduction

The first research on the asymptotic coarsening behavior of the size distribution of spherical particles, and on the associated power laws for the average radius of particles, matrix supersaturation and number density of particles has been carried out independently by Lifshitz and Slyozov [1] and Wagner [2] (LSW). They considered a two-phase system consisting of a vanishingly small volume fraction of a dispersed phase. Based on the LSW theory, Ardell [3] has derived a time law for the matrix supersaturation surrounding a spherical particle. Recently, Kuehmann and Voorhees (KV) [4] have developed a theory for the coarsening of a spherical precipitated phase having two chemical components in a ternary alloy. By formulating the Gibbs-Thomson equation for the ternary system, they found that the temporal power laws of the average particle radius, far-field-matrix supersaturation and particle number density were identical to those of the LSW theory but the amplitudes of these power laws were different from the LSW theory. The theories of LSW, LSW modified by Ardell, and KV have already been employed to study the Ostwald ripening processes of spherical second-phase precipitates in actual alloys [5-9]. However, the actual shapes of second-phase particles are usually non-spherical. It is thus useful to generalize the KV theory for any shape of particles.

Several studies have been experimentally performed on the growth kinetics of spherical fcc Co and γ-Fe precipitates in Cu-Co [10-13] and Cu-Fe alloys [14]. The experimental studies by saturation magnetization measurements [10] and transmission electron microscopy (TEM) [11-14] have revealed that the average radii of Co and γ-Fe precipitates increase with t as $t1/3$, in accord with the prediction of the LSW theory. Using experimental values of the precipitate growth rate and literature data on the diffusivity and solubility limit of solutes, Seno et al. [12] and Matsuura et al. [14] have estimated the interface energies γ of Co and γ-Fe precipitates as about 0.31 and 0.25 Jm-2, respectively. On the other hands, Oriani [15] and Ardell and Nicholson [16] have obtained $\gamma \approx 0.3$ to 1.0 Jm-2 from analyses of Livingston's

data [10] with available values of the diffusivity and solubility limit of Co in Cu.

Recently, we have examined the coarsening behavior of Co precipitates in Cu-1, 2 and 4wt%Co alloys aged at temperatures of 873, 923 and 973 K by both of TEM observations and electrical resistivity measurements [17-19]. The shape of Co precipitates changes from a sphere to an octahedron faceted on the matrix {111} via a cube with {001} as the precipitates grow. For non-spherical precipitates, the radius of a sphere with volume identical to that of the non-spherical precipitate was calculated. The values of $\gamma \approx 0.15$ Jm^{-2} for spherical Co precipitates and the diffusion coefficient of Co in the Cu matrix were derived independently from data on coarsening alone using the LSW theory. On the other hand, Monzen and Kita [20] have investigated the coarsening of γ-Fe precipitates in Cu-1.0 and 1.7wt%Fe alloys during aging at 873 to 973 K by the same method as above, supposing that the precipitate shape is spherical. By applying the LSW theory to the experimental data, the value of $\gamma \approx 0.25$ Jm^{-2} was estimated. Watanabe et al. [18] have also studied the Ostwald ripening of γ-Fe precipitates in a Cu-2.0wt%Fe alloy aged at 773 and 973 K. The estimate of γ was 0.27 Jm^{-2} from the same approach as Monzen and Kita [20]. The shape of γ-Fe precipitates changes from a sphere to a cube with {001} facets, similar to the observation of Cu-Co alloys. The radius of a sphere with the same volume as that of the cube was used to calculate γ.

Aging of Cu-base alloys containing Co and Fe produces first spherical coherent Co-Fe precipitates with a fcc structure [21-23]. We have studied the coarsening of Co-Fe precipitates in a ternary Cu-1.47wt%Co-0.56wt%Fe alloy aged at 873 to 973 K [24]. Observations by TEM and electrical resistivity measurements were performed in order to describe the microstructural evolution and concentration of solute in the Cu matrix. The composition of Co-Fe precipitates was found to be 70at%Co-30at%Fe, which is consistent with the ratio of atomic amounts of Co and Fe in the alloy. As in the case of Cu-Co binary alloys, there existed three precipitate shapes: a sphere, a cube with {001} facets and an octahedron faceted on {111}. The cube or octahedron was reduced to an equivalent-volume sphere. Independent values of γ and the

diffusivity of Co and Fe in the matrix have been determined using the KV theory. The obtained values of γ were about 0.20 Jm^{-2}, which lies between the reported values of $\gamma \approx 0.15$ Jm^{-2} for Cu-Co alloys [17-19] and $\gamma \approx 0.26$ Jm^{-2} for Cu-Fe alloys [18, 20].

In this study, we will first extend the KV theory to a general case of second-phase particle with any centro-symmetric shape. In the generalized KV (GKV) theory, it is assumed that the particle shape is determined by minimization of the interface energy. We will show from a thermodynamic analysis that a correct energy of any interface of the second-phase particle can be estimated by application of the GKV theory even when the particle shape is not governed by the interface energy minimization, that is, it is affected by the misfit strain energy, originating from misfit between the matrix and particle. In addition, the Ostwald ripening of Co-Fe precipitates in Cu-1.01wt%Co-1.04wt%Fe and Cu-0.63wt%Co-1.33wt%Fe alloys aged at 873, 923 and 973 K is examined by TEM and electrical resistivity measurements. Finally, the interface energies for spherical, cuboidal and octahedral precipitates in the two Cu-Co-Fe, the Cu-1.47wt%Co-0.56wt%Fe [24], the Cu-2wt%Co [19] and the Cu-1.7wt%Fe alloys [20] are determined using the GKV theory.

2. Generalization of KV theory

2. 1 Geometric description

A crystalline solid will, in general, have a specific interface energy which varies with the orientation of the surface relative to the crystal axes: if surface orientation is denoted by the unit normal to the surface $\boldsymbol{n}$, the specific interface energy γ is expressed as a function $\gamma(\boldsymbol{n})$. The construction given by Wulff [25] determines the shape which, for given $\gamma(\boldsymbol{n})$ and fixed volume, has the least interface energy. Wulff theorem states that the normal distance, measured from a fixed origin, of a surface element on a particle is proportional to $\gamma(\boldsymbol{n})$ of the element. Supposing

that values of γ_0 (=$\gamma(\boldsymbol{n}_0)$) and λ_0 (=$\lambda(\boldsymbol{n}_0)$) are known, the Gibbs-Thomson equation (GTE) generalized to any particle with 3-dimensionally-point symmetric shape [26] is

$$\mu_{\mathrm{m}}(\lambda_0) - \mu_{\mathrm{m}}(\infty) = \frac{2\gamma_0}{\lambda_0} V_{\mathrm{m}} = \frac{2\gamma(\boldsymbol{n})}{\lambda(\boldsymbol{n})} V_{\mathrm{m}} \tag{1}$$

where $\lambda(\boldsymbol{n}) = \boldsymbol{l}(\boldsymbol{n}) \cdot \boldsymbol{n}$, $\boldsymbol{l}(\boldsymbol{n})$ is the vector drawn from the center of symmetry to a surface element, $\mu_{\mathrm{m}}(\lambda_0)$ is the chemical potential of the matrix or α phase in equilibrium with a β particle of length λ_0, $\mu_{\mathrm{m}}(\infty)$ is that of the matrix in equilibrium with a flat surface of the same substance, and V_{m} is the molar volume of β phase. The unit of the chemical potential is joule per mole. A closed surface characterized by the vectors $\boldsymbol{n}$ and $\boldsymbol{l}(\boldsymbol{n})$ is so-called γ-plot. The particle shape is set to remain unchanged since the generalized GTE is derived under the shape equilibrium condition. The geometry of the system considered here is presented schematically in Fig. 1. Using a value of λ_0, the surface area S_{a} and volume V of the β particle are written as

$$S_{\mathrm{a}} = \eta \lambda_0^2 \tag{2}$$

$$V = \omega \lambda_0^3 \tag{3}$$

where η and ω are particle-shape-dependent constants. For example, η=4π and ω=4π/3 for a spherical particle. Hereafter the non-spherical particle illustrated in Fig. 1 is referred to as general particle. Though the $\lambda(\boldsymbol{n})$ is not always coincident with the particle size as shown in Fig. 1, $\lambda(\boldsymbol{n})$ will be called particle size.

2. 2 Kinetic equation

Let us consider a ternary system, consisting of solvent (1) and two solutes (2 and 3). At first, the solute concentration profile should be defined. Since the ratio $\gamma(\boldsymbol{n}) / \lambda(\boldsymbol{n})$ in Eq. (1) is constant for all interface orientations of a general particle, the solute concentration in the matrix near a α/β interface is the same over the whole surface of the β particle [26, 27]. Thus, we consider the equivalent-volume sphere (EVS) for the representation of the concentration

field. In this paper, the units of concentration terms will be taken as atomic fraction. The concentration field of the α phase can be written with respect to the λ_0 as

$$C_i^{\alpha}(\lambda) = C_i^{\infty} + \left(\hat{C}_i^{\alpha} - C_i^{\infty}\right)\frac{\lambda_0}{\lambda} \quad (i = 2, 3) \tag{4}$$

where $C_i^{\alpha}(\lambda)$ is the solute concentration of the component *i* in the matrix at distance λ from the center of β, C_i^{∞} is the composition of the component *i* in α phase at infinity and $\hat{C}_i^{\alpha}$ is the matrix concentration of the *i*th component at the α/β interface. Here we neglect off-diagonal terms in the diffusion matrix. Eq. (4) is, of course, a harmonic function and is also obtained from the composition profile in the KV coarsening theory by replacing the radial variable and particle radius by λ and λ_0.

The mass conservation at the non-spherical interface is

$$\left(\hat{C}_i^{\beta} - \hat{C}_i^{\alpha}\right)\frac{dV}{dt} = S_{\mathrm{a}} J_i \tag{5}$$

where $\hat{C}_i^{\beta}$ is the composition of the component *i* in the β phase at the α/β interface, *t* is the time and J_i is the diffusion flux of the *i*th component. Eqs. (2) to (5) and Fickian law yield the relation between the growth rate $d\lambda_0/dt$ of the general particle and the matrix concentration:

$$\left(\hat{C}_i^{\beta} - \hat{C}_i^{\alpha}\right)\frac{d\lambda_0}{dt} = \left(\frac{\eta}{3\omega}\right) D_i \left\{\frac{\partial C_i^{\alpha}(\lambda)}{\partial \lambda}\right\}_{\lambda=\lambda_0} \tag{6}$$

Here D_i is the diffusion coefficient of the *i*th component in the α phase. Following KV [4], we assume to a good approximation during ripening that $\hat{C}_i^{\beta} - \hat{C}_i^{\alpha} \approx C_i^{\beta} - C_i^{\alpha} = \Delta C_i$, where C_i^{α} and C_i^{β} are the equilibrium solubilities of the component *i* in the α and β phases. From Eqs. (4) and (6) with *i* = 2 and 3, we have

$$\frac{\left(\hat{C}_2^{\alpha} - C_2^{\infty}\right)}{\left(\hat{C}_3^{\alpha} - C_3^{\infty}\right)}\frac{D_2}{D_3} = \frac{\Delta C_2}{\Delta C_3} \tag{7}$$

Eq. (7) is equal to the result obtained by Kuehmann and Voorhees [4].

Next, we will develop the GTE for the general particle in the ternary system, to

express the $d\lambda_0/dt$ as a function of the matrix far-field concentration and the size λ_0. The GTE for a spherical particle has already been obtained by KV [4]. According to KV, we have the GTE for the general particle as

$$\hat{C}_2^\alpha - C_2^\alpha = \frac{\Delta C_2}{D_2}\frac{2\gamma_0 V_m}{\Lambda}\frac{1}{\lambda_0} + \frac{\left(\Delta C_2 G_{23}^\alpha + \Delta C_3 G_{33}^\alpha\right)}{\Lambda}\left\{\frac{\Delta C_3}{D_3}\left(C_2^\infty - C_2^\alpha\right) - \frac{\Delta C_2}{D_2}\left(C_3^\infty - C_3^\alpha\right)\right\} \quad (8)$$

$$\hat{C}_3^\alpha - C_3^\alpha = \frac{\Delta C_3}{D_3}\frac{2\gamma_0 V_m}{\Lambda}\frac{1}{\lambda_0} + \frac{\left(\Delta C_2 G_{22}^\alpha + \Delta C_3 G_{23}^\alpha\right)}{\Lambda}\left\{-\frac{\Delta C_3}{D_3}\left(C_2^\infty - C_2^\alpha\right) + \frac{\Delta C_2}{D_2}\left(C_3^\infty - C_3^\alpha\right)\right\} \quad (9)$$

from Eqs. (1) and (7) and usual thermodynamic treatments. Here

$\Lambda = \frac{\Delta C_2}{D_2}\left(\Delta C_2 G_{22}^\alpha + \Delta C_3 G_{23}^\alpha\right) + \frac{\Delta C_3}{D_3}\left(\Delta C_2 G_{23}^\alpha + \Delta C_3 G_{33}^\alpha\right)$, $G_{ij}^\alpha = \frac{\partial G^\alpha}{\partial C_i^\alpha \partial C_j^\alpha}$ (i or j = 2 and 3) and G^α is the Gibbs free energy of the α phase. The units of G^α and G_{ij}^α are joule per mole, the same as that of the chemical potential. The capillary length L_{ci} of the component i is given by $L_{ci} = \frac{\Delta C_i}{D_i}\frac{2\gamma_0 V_m}{\Lambda}$. Using Eqs. (4) and (6) with i = 2 or 3 and Eq. (8) or (9), the particle growth rate $d\lambda_0/dt$ ($\equiv \dot{\lambda}_0$) is related to the size λ_0 and the supersaturations at infinity as

$$\dot{\lambda}_0 = \left(\frac{\eta}{3\omega}\right)\frac{1}{\lambda_0 \Lambda}\left\{\left(\Delta C_2 G_{22}^\alpha + \Delta C_3 G_{23}^\alpha\right)\left(C_2^\infty - C_2^\alpha\right) + \left(\Delta C_2 G_{23}^\alpha + \Delta C_3 G_{33}^\alpha\right)\left(C_3^\infty - C_3^\alpha\right) - \frac{2\gamma_0 V_m}{\lambda_0}\right\} \quad (10)$$

For a sphere, η=4π and ω=4π/3, and λ_0 and γ_0 correspond to the radius and the isotropic interface energy of the sphere.

2. 3 Asymptotic solution

As shown in the Appendix A, the mathematical treatments to obtain asymptotic solutions are quite similar to those found by Voorhees [28]. Thus, we will only state the results of this analysis. With replacements of λ_0 and γ_0 by $\lambda(\boldsymbol{n})$ and $\gamma(\boldsymbol{n})$, in the limit $t \to \infty$

$$\overline{\lambda}(\boldsymbol{n})^3 = K_n t \quad (11)$$

$$K_n = \left(\frac{\eta}{3\omega}\right)\frac{8\gamma(\boldsymbol{n})V_{\mathrm{m}}}{9\Lambda} \tag{12}$$

where $\bar{\lambda}(\boldsymbol{n})$ is the average particle size and K_n is the coarsening rate constant. The far-field supersaturation for the component i is

$$C_i^{\infty} - C_i^{\alpha} = k_{n,i} t^{-1/3} \tag{13}$$

$$k_{n,i} = \left(\frac{3\omega}{\eta}\right)^{1/3} \frac{\left(3\gamma(\boldsymbol{n})V_{\mathrm{m}}\right)^{2/3}\Lambda^{1/3}C_i^{\alpha}}{\left(\Delta C_2 G_{22}^{\alpha} + \Delta C_3 G_{23}^{\alpha}\right)C_2^{\alpha} + \left(\Delta C_2 G_{23}^{\alpha} + \Delta C_3 G_{33}^{\alpha}\right)C_3^{\alpha}} \tag{14}$$

Here $k_{n,i}$ is the coarsening parameter. The number of particles per unit volume F is written as

$$F(t) \cong \frac{\phi_{\mathrm{eq}}}{4.74K_n} t^{-1} \tag{15}$$

where ϕ_{eq} is the equilibrium volume fraction of particles. In the derivation of Eq. (15), the well-known size distribution $g(u)$ ($u=\lambda(\boldsymbol{n})/\bar{\lambda}(\boldsymbol{n})$) of the LSW theory [29] is required [28]. Thus, the size distribution of the general particle is identical to that predicted from the LSW theory for spherical particle. Finally, we now summarize the assumptions for application of the GKV theory: (i) the particle shape remains unchanged during coarsening, and (ii) the system is a dilute solution.

3. Evaluation of $\gamma(\boldsymbol{n})$ for non-spherical particles

In the GKV theory, the Wulff construction is supposed to be valid: that is, (a) the shape of a particle is determined by the minimum interface-energy criterion and (b) $\gamma(\boldsymbol{n})$ is proportional to $\lambda(\boldsymbol{n})$. However, there generally exists the elastic strain energy due to misfit between α and β phases in crystalline solids. Onaka et al. [30] have theoretically and experimentally shown that the particle shape is determined so as to minimize the sum of the elastic strain and interface energies of a β particle, indicating that the above hypothesis (a) is not valid in actual alloy systems. We will show that even if the assumption (a) is incorrect, the

assumption (b) holds true and thus the proper $\gamma(\boldsymbol{n})$ can be estimated from the GKV theory.

It has been theoretically shown that the elastic interaction of two or more particles affects the coarsening kinetics [31, 32]. In the thermodynamic analysis below, however, the elastic interaction energy will not be taken into consideration since the GKV theory should be applied in dilute systems, where the volume fraction of β particles is very small.

We will first obtain the local equilibrium condition for a system with the elastic strain energy. The general strategy [33] for finding conditions for the local equilibrium is applied to a system consisting of α and β phases, containing 3 components each and separated by curved interfaces. Here, β particles are set to have a given shape with a smooth surface. Let us define the superficial excess value for any properties. Using the symbol I for U, S, V and n_i, the superficial excess value I^s for I is given by

$$I^s \equiv \frac{I_{sys} - \left(I^\alpha + I^\beta\right)}{A_{sys}} \tag{16}$$

where U, S, V and n_i are the internal energy, entropy, volume and number of moles of the component i of the α or β phase, A_{sys} is the surface area and I_{sys} is the value I of the system. An expression for the change in entropy of the system is written as

$$dS_{sys} = \left(\frac{dU^\alpha}{T^\alpha} + \frac{P^\alpha}{T^\alpha}dV^\alpha - \sum_{i=1}^{3}\frac{\mu_i^\alpha}{T^\alpha}dn_i^\alpha\right) + \left(\frac{dU^\beta}{T^\beta} + \frac{P^\beta}{T^\beta}dV^\beta - \frac{E}{T^\beta}dV^\beta - \sum_{i=1}^{3}\frac{\mu_i^\beta}{T^\beta}dn_i^\beta\right) + S^s dA_{sys} \tag{17}$$

where T, P and μ_i are the temperature, pressure and chemical potential of the ith component of the α or β phase, and E is the elastic strain energy per unit volume, dependent only on the shape of β. When the α phase is elastically isotropic and the β phase has arbitrary uniform misfit strains, Eshelby [34] has revealed from the ellipsoidal inclusion problem that the total elastic strain energy in the system can be written in the form of EV^β. This problem has been extended to the case that the α phase is elastically anisotropic [30, 35, 36]. In this case also, the elastic energy can be expressed in the same fashion. The internal energy, volume and total number of moles of each component are constant in an isolated system with internal interfaces.

These constraints may be written as

$$dU_{\mathrm{sys}} = 0 = dU^{\alpha} + dU^{\beta} + U^{s} dA_{\mathrm{sys}} \tag{18}$$

$$dV_{\mathrm{sys}} = 0 = dV^{\alpha} + dV^{\beta} + V^{s} dA_{\mathrm{sys}} \tag{19}$$

$$dn_{i,\mathrm{sys}} = 0 = dn_i^{\alpha} + dn_i^{\beta} + n_i^{s} dA_{\mathrm{sys}} \tag{20}$$

Here V^s is zero [33]. Let the curvature of the interface be defined to be positive when the interface is convex relative to the β phase. Assuming that the surface of the β particle is hypothetically divided into p small elements, the increment in surface area δA_e of eth surface element as β grows is related to the increment in the volume δV_e^{β} of the eth element and the local mean curvature H_e of the eth element as

$$\delta A_e = 2 H_e \delta V_e^{\beta} \tag{21}$$

Substituting Eqs. (18) to (21) into Eq. (17) and all the coefficients of the differentials in Eq. (17) being equal to zero with relations of $\sum_{e=1}^{p} \delta A_e = dA_{\mathrm{sys}}$ and $\sum_{e=1}^{p} \delta V_e^{\beta} = dV^{\beta} = -dV^{\alpha}$, we have the conditions for the local equilibrium. If α and β are maintained in the local equilibrium as the state of the system is altered, the conditions require that

$$dT^{\alpha} = dT^{\beta} \tag{22}$$

$$dP^{\beta} - dP^{\alpha} = \frac{2 \sum_{e=1}^{p} \gamma_e \sum_{e=1}^{p} \left(dH_e \delta V_e^{\beta} \right)}{\sum_{e=1}^{p} \delta V_e^{\beta}} \tag{23}$$

$$d\mu_i^{\alpha} = d\mu_i^{\beta} \tag{24}$$

Here γ_e is the interface energy of the eth element. The infinitesimal change in the Gibbs energy G of the α and β phases are given by

$$dG^{\alpha} = -S^{\alpha} dT^{\alpha} + V^{\alpha} dP^{\alpha} + \sum_{i=1}^{3} \mu_i^{\alpha} dn_i^{\alpha} \tag{25}$$

$$dG^{\beta} = -S^{\beta} dT^{\beta} + V^{\beta} dP^{\beta} + E dV^{\beta} + \sum_{i=1}^{3} \mu_i^{\beta} dn_i^{\beta} \tag{26}$$

The units of G^{α} and G^{β} are not joule per mole but joule since we here focus on the transfer of molecules in the system. To consider the partial molar Gibbs energy for the ith component, we estimate the partial derivatives of G^{α} and G^{β} with respect to n_i^{α} and n_i^{β} from Eqs. (25) and

(26) under the condition that temperature, pressure and n_j^{α} and n_j^{β} ($j \neq i$) are held constant. This leads to the following expression:

$$\sum_{i=1}^{3}\left(\mu_{ij}^{\alpha} dC_{c,j}^{\alpha} - \mu_{ij}^{\beta} dC_{c,j}^{\beta}\right) = \frac{2\sum_{e=1}^{p}\gamma_e \sum_{e=1}^{p}\left(dH_e \delta V_e^{\beta}\right)}{\sum_{e=1}^{p}\delta V_e^{\beta}} \overline{V}_i^{\beta} \qquad (27)$$

by using Eqs. (22) to (24), considering the minimal change in the partial molar Gibbs energy under the isothermal condition, and assuming that $dP^{\alpha} \approx 0$. In this process, since the partial molar volume $\overline{V}_i^{\beta}$ for the component *i* in the β phase can be regarded as a constant value from its definition [33], the term $d\left(E\overline{V}_i^{\beta}\right)=0$. Here the coefficient $\mu_{ij} \equiv \frac{\partial \mu_i}{\partial C_{c,j}}$ (j = 1, 2 and 3) shows the change in chemical potential of the component *i* with composition $C_{c,j}$ in the α or β phase [33]. Eq. (27) means that the coarsening of the *e*th surface element at a constant temperature is driven by the γ_e. From this result, together with the shape similarity of the β particle during coarsening, we find that relative values of $\gamma(\boldsymbol{n})$ are proportional to those of $\lambda(\boldsymbol{n})$ even when the assumption (a) for the Wulff construction that the shape of a particle is determined by minimization of the interface energy does not hold true in actual systems. This result also indicates that the elastic strain energy has no effect on the coarsening kinetics, in agreement with our intuition.

4. Coarsening of Co-Fe precipitates in ternary Cu-Co-Fe alloys

4. 1 Experimental

Ingots of Cu-1.01wt%Co-1.04wt%Fe and Cu-0.63wt%Co-1.33wt%Fe alloys were prepared by melting 99.99wt%Cu, a Cu-10.5wt%Co and a Cu-10.0wt%Fe master alloy. The atomic Co/Fe ratios of these alloys are 1:1 and 3:7. The total atomic amounts of Co and Fe in

the two alloys are about 2.2%, which is identical to 2.2% in a Cu-1.47wt%Co-0.56wt%Fe alloy used in our previous study [24]. Hereafter, the compositions of the alloys will be expressed in atomic percent. The alloy ingots were homogenized at 1173 K for 24 h in a vacuum. Specimen pieces were cut from the ingots and cold-rolled to a thickness of 3 mm. Then the specimens were solution-treated at 1303 K for 5 h in a vacuum, quenched into cold water (273 K), and subsequently aged at 873, 923 and 973 K in a vacuum.

Thin foils, 0.2 mm thick, for TEM observations were prepared from the aged specimens by electropolishing using a 20vol% solution of a phosphoric acid in water. Microscopy was performed using a JEOL 2010FEF and a JEOL 2000EX or a HITACHI H-9000NAR microscope at an operation voltage of 200 or 300 kV, and equipped with an energy dispersive X-ray spectroscopy (EDX) system.

The solution-treated specimens for electrical resistivity measurements were spark-cut to the size of 100 mm x 10 mm x 0.5 mm. After aging, resistivity measurements were made at 293 K using a standard four-point potentiometric technique. The cross-sectional area of the specimen was measured at different positions and the average value was used. By applying the experimental data obtained by Linde [37], the Co and Fe concentrations in the Cu matrix were determined.

4. 2 Experimental results

4. 2. 1 Precipitated phase

As in our previous paper [24], an EDX analysis was carried out to examine the chemical composition of Co-Fe precipitates in Cu-0.68at%Co-1.52at%Fe and Cu-1.09at%Co-1.16at%Fe specimens aged at 973 K for 10 min and 48 h, using the beam directed at Co-Fe precipitates. For each specimen, when the detected concentrations of Co and

Fe were plotted against Cu concentration, a linear relationship was observed, as shown in Fig. 2. Cu atoms were always detected, as seen in Fig. 2. Thus, in order to exclude the effect of Cu, from the intercepts of the straight lines drawn by the least-squares method, the Co and Fe concentrations in the precipitates were determined. The Co and Fe concentrations in atomic fraction were 0.30 and 0.70 for the Cu-0.68Co-1.52Fe alloy, 0.50 and 0.50 for the Cu-1.09Co-1.16Fe alloy, and 0.70 and 0.30 for the Cu-1.58Co-0.64Fe alloy [24], independent of aging temperature and time. These ratios are consistent with the ratios of atomic amounts of Co and Fe in the alloys.

Figs. 3 and 4 depict bright-field images of Co-Fe precipitates in Cu-0.68Co-1.52Fe and Cu-1.09Co-1.16Fe alloys aged at 973 K, taken using the matrix [001] zone axis. The insets at the lower right in Figs. 3 and 4 are selected-area diffraction patterns (SADPs) taken from the areas containing Co-Fe precipitates. Extensive analyses of the SADPs of the Cu-0.68Co-1.52Fe specimen revealed that the precipitated phase had a disordered fcc structure with the cube-on-cube orientation relationship to the Cu matrix. In the SADPs in Fig. 4, there are extra reflections of precipitates, which possess a banded structure. Analyses of the SADPs taken using the {111} zone axis showed that the layered internal structure consisted of two twin-related bcc Co-Fe variants, and the Kurdjumov-Sachs orientation relationship was satisfied between both of these two variants and the Cu matrix. This relationship is in agreement with the reported relationship between the Cu matrix and α-Fe martensite precipitates in deformed Cu-Fe binary alloys [38]. Monzen and Kato [23] have found that the ternary addition of Co to a Cu-Fe alloy tends to destabilize the fcc Co-Fe precipitates and, thus, the fcc-to-bcc martensitic transformation in Co-Fe precipitates can occur by simple cooling and the transformed precipitates are internally twinned. They have further shown that as the Co content in Cu-Co-Fe alloys increases, the transformation temperature increases, reaching a maximum for the Co/Fe ratio = 1:1 and then decreases again. The cooling temperature at which all Co-Fe precipitates larger than about 10 nm in diameter in a Cu-Co-Fe alloy with Co/Fe =

1:1 are martensitically transformed is about 323 K. Therefore, it is stated that the Co-Fe precipitates in the Cu-1.09Co-1.16Fe alloy have the fcc structure with the cube-on-cube relationship to the Cu matrix during aging at 873 to 973 K, and the fcc-to-bcc martensitic transformation occurs during cooling up to 273 K.

Small Co-Fe precipitates in the Cu-0.68Co-1.52Fe and Cu-1.09Co-1.16Fe alloys were spherical, as clearly recognized from a bright-field image inserted in Fig. 3(a), and a dark-field image inserted in Fig. 4(a), taken using a reflection of the bcc Co-Fe precipitates. The shapes of large precipitates in both the alloys were nearly cuboidal with flat interfaces parallel to {001}, as seen in Figs. 3(b) and 4(b). Fringes around the precipitates in Fig. 3(b) are noticed. Although we did not analyze the fringes in detail, they may be δ-fringe christened by Ardell [39]. The spherical-to-cuboidal shape transitions have been reported in aged Cu-Co-Cr [40], Cu-Co [17-19] and Cu-Fe alloys [18]. When r is taken as the radius of EVS, cuboidal precipitates existed above $r \approx 10$, 10, 15, 20 and 25 nm for Cu-2.15Co [19], Cu-1.58Co-0.64Fe, Cu-1.09Co-1.16Fe, Cu-0.68Co-1.52Fe and Cu-1.93Fe alloys. There were octahedral precipitates above $r \approx 30$ and 40 nm for Cu-2.15Co [19] and Cu-1.58Co-0.64Fe alloys.

4. 2. 2 Kinetics of Co-Fe precipitates during Ostwald ripening

Eqs. (11) and (12) indicate that log-log plots of $\bar{\lambda}(n)$ versus t yield time exponents. Fig. 5 displays the average precipitate size $\bar{\lambda}(n)$ against aging time t on logarithmic scales for Cu-0.68Co-1.52Fe and Cu-1.09Co-1.16Fe alloys. Excepting at early times, the experimental slopes are almost identical to the value of 1/3 for spherical and cuboidal precipitates, predicted by the GKV theory. Log-log plots of $\bar{\lambda}(n)$ versus t using data in the literature [19, 20, 24] reveal that the $\bar{\lambda}(n)$ for octahedral precipitates in the Cu-2.15Co and Cu-1.58Co-0.64Fe alloys, and cuboidal precipitates in the Cu-2.15Co, Cu-1.58Co-0.64Fe and Cu-1.93Fe alloys obeys the $t^{1/3}$ law. Fig. 6 shows the coarsening curves of Co-Fe precipitates in the

Cu-0.68Co-1.52Fe alloy aged at 873, 923 and 973 K. For each temperature and shape, a linear relationship exists between $\bar{\lambda}(\boldsymbol{n})^3$ and *t*. It should be also noted in Figs. 5 and 6 that, for each alloy and temperature, experimental points for sphere and EVS lie on the identical straight line, even when the shape transition occurs. This held for the five alloys. This will be discussed in section 5. 1. Experimental values of the rate constant K_n were determined from the slopes of the straight lines by the least-squares method. The K_n for sphere and EVS, cube and octahedron will be referred to as K_s, K_{001} and K_{111}, respectively. Table 1 lists the values of K_n for the present two alloys, together with the values calculated from size data for the Cu-2.15Co [19], Cu-1.58Co-0.64Fe [24] and Cu-1.93Fe [20] alloys.

For each alloy and temperature, the growth rate has decreased gradually with *t* at the initial stage of aging, and, after a certain time, a linear relationship has been observed between $\bar{\lambda}(\boldsymbol{n})^3$ and *t*, although the rate changes cannot be obviously seen in Fig. 6. In our previous papers, we showed evidence for a mixed stage of growth and coarsening of Co and Co-Fe precipitates in the Cu-1.08Co [17] and Cu-1.58Co-0.64Fe [24] alloys before the beginning of a coarsening stage. In addition, we found that the transitions from the mixed stage of growth and coarsening to the coarsening stage changed the growth rates of the Co and Co-Fe precipitates at early times. Similarly, the rate changes in the present study have been found to be caused by the transitions from the mixed stage to the coarsening stage.

As described in section 2. 3, the size distributions of 3-dimensionally-point symmetric particles in ternary systems follow the distribution function $g(u)$ ($u=\lambda(\boldsymbol{n})/\bar{\lambda}(\boldsymbol{n})$) of the LSW theory. A comparison between the measured and the theoretically predicted size distributions is shown in Fig. 7. The agreement between the experimental distributions of small spherical precipitates and the theoretical curves is relatively good. However, the distributions of larger cuboidal and octahedral precipitates are broader than the predicted curves. The broader bottom-shapes of histograms of larger precipitates are similar to those predicted by the theories of Ardell [41], Voorhees and Glicksman [42] and Wang et al. [43], considering the effect of

precipitate volume fraction on coarsening. The experimental broad distributions are also consistent with those in Cu-Co and Cu-Fe alloys reported by Seno et al. [12] and Matsuura et al. [14].

4. 2. 3 Change in solute concentration in Cu matrix

The atomic Co/Fe ratios of the precipitates are 3:7 and 1:1 for the Cu-0.68Co-1.52Fe and Cu-1.09Co-1.16Fe alloys, independent of aging temperature and time, as described in section 4. 2. 1. The solute concentrations of Co and Fe in the Cu matrix were obtained by the electrical resistivity method, taking the ratio of Co/Fe into account.

Following Eqs. (13) and (14), C_{i}^{∞} versus $t^{-1/3}$ was plotted for the two alloys aged at 873, 923 and 973 K. For each aging temperature and solute, C_{i}^{∞} exhibited a steep decrease in the initial stage of aging as illustrated by a dashed line, and, after a certain time, a linear relationship was seen between C_{i}^{∞} and $t^{-1/3}$, as exemplified in Fig. 8. The slopes of these lines give experimental values of $k_{n,\mathrm{i}}$. Although $k_{n,\mathrm{i}}$ depends on the precipitate shape, according to Eq. (14), clear shape dependence of $k_{n,\mathrm{i}}$ was not detected. Table 2 lists the values of $k_{n,\mathrm{i}}$ for the two alloys, determined by the least-squares fits, together with the reported values for the Cu-Co [19], Cu-Co-Fe [24] and Cu-Fe [20] alloys. Also extrapolation to $t^{-1/3}=0$ yields values of C_{i}^{α}. Table 3 summarizes these values, along with the reported values of equilibrium solubility for the Cu-Co [17], Cu-Co-Fe [24] and Cu-Fe [20] alloys. The obtained values of C_{Co}^{α} and C_{Fe}^{α} in the ternary alloys are smaller than the reported solubilities of Co and Fe in binary alloys. However, this is in agreement with the calculated result of the Cu-Co-Fe ternary equibrium diagrams [44] that the simultaneous dissolution of Co and Fe into Cu reduces the solubility of both Co and Fe in Cu.

Eq. (15) indicates that the number density F decreases with t as t^{-1}. Log-log plots of F versus t for the Cu-0.68Co-1.52Fe alloy are presented in Fig. 9. The values of F were obtained

from $F = 3\phi/(4\pi r^3)$, where ϕ is the volume fraction of the precipitated phase at time t. Values of ϕ were calculated from $\phi = \left(C_{0,\mathrm{i}}^{\alpha} - C_{\mathrm{i}}^{\infty}\right)/\left(C_{\mathrm{i}}^{\beta} - C_{\mathrm{i}}^{\alpha}\right)$, where $C_{0,\mathrm{i}}^{\alpha}$ is the matrix concentration of the component i after solutionizing. The time dependence of F in Eq. (15) is obtained in the long-time limit, namely a system with a constant ϕ. On the other hand, Ardell [45] has considered the temporal behavior of the precipitate number density during coarsening when ϕ varies with time. In this case, the relation between F and t in 3-dimension ripening and diffusion is written by the form

$$F = \Xi t^{-1} - \Omega t^{-4/3} \tag{28}$$

where Ξ and Ω are constants. The theoretical values of F calculated from Eq. (28), using $\phi_{\mathrm{eq}} \approx 0.018$, our values of K_{s} and C_{i}^{α}, available data on the diffusivity of Co in Cu [46] and appropriate constants in Ardell's paper [45], are also shown by the straight lines in Fig. 9. The slopes of the straight lines are almost equal to -1. For each temperature, the data points for sphere and cube lie on the straight line, except for the initial stage of aging. It was recognized that, for each alloy and temperature, F decreased with t as t^{-1}, irrespective of the precipitate shape.

5. Discussion

5. 1 Calculation of $\gamma(\boldsymbol{n})$ from experimental data

Combination of the K_n, $k_{n,\mathrm{i}}$ C_{Co}^{α} and C_{Fe}^{α} enables the matrix / precipitate interface energy $\gamma(\boldsymbol{n})$ to be calculated without having to assume values of D_{Co} and D_{Fe}, namely

$$\gamma(\boldsymbol{n}) = \frac{K_n^{1/3} k_{n,\mathrm{Co}}}{2V_{\mathrm{m}} C_{\mathrm{Co}}^{\alpha}} \left\{ \left(\Delta C_{\mathrm{Co}} G_{\mathrm{CoCo}}^{\alpha} + \Delta C_{\mathrm{Fe}} G_{\mathrm{CoFe}}^{\alpha}\right) C_{\mathrm{Co}}^{\alpha} + \left(\Delta C_{\mathrm{Co}} G_{\mathrm{CoFe}}^{\alpha} + \Delta C_{\mathrm{Fe}} G_{\mathrm{FeFe}}^{\alpha}\right) C_{\mathrm{Fe}}^{\alpha} \right\} \tag{29}$$

The value of V_{m} was calculated as 6.8 x 10^{-6} $\mathrm{m^3 mol^{-1}}$ from $V_{\mathrm{m}} = N_{\mathrm{a}} a^3/4$, where N_{a} is the Avogadro's number and a is the lattice constant of fcc Fe phase (=0.3562 nm [38]). The lattice

parameters of fcc Co [47], fcc Co-Fe [48] and fcc Fe [38] phases are almost identical. Using the subregular solution model, we have the following expressions during aging:

$$G^{\alpha}_{\mathrm{CoCo}} = RT\left(\frac{1}{C^{\infty}_{\mathrm{Co}}} + \frac{1}{1-C^{\infty}_{\mathrm{Co}}-C^{\infty}_{\mathrm{Fe}}}\right) - 2L_{\mathrm{CuCo}} - 2L_{\mathrm{CuCoFe}}C^{\infty}_{\mathrm{Fe}} \tag{30}$$

$$G^{\alpha}_{\mathrm{CoFe}} = \frac{RT}{1-C^{\infty}_{\mathrm{Co}}-C^{\infty}_{\mathrm{Fe}}} - L_{\mathrm{CuCo}} + L_{\mathrm{CoFe}} - L_{\mathrm{FeCu}} + L_{\mathrm{CuCoFe}}\left(1-2C^{\infty}_{\mathrm{Co}}-2C^{\infty}_{\mathrm{Fe}}\right) \tag{31}$$

$$G^{\alpha}_{\mathrm{FeFe}} = RT\left(\frac{1}{1-C^{\infty}_{\mathrm{Co}}-C^{\infty}_{\mathrm{Fe}}} + \frac{1}{C^{\infty}_{\mathrm{Fe}}}\right) - 2L_{\mathrm{FeCu}} - 2L_{\mathrm{CuCoFe}}C^{\infty}_{\mathrm{Co}} \tag{32}$$

where R is the gas constant, L_{ij} is the interaction parameter between i and j atoms (i or j = Cu, Co and Fe), and L_{CuCoFe} is the ternary interaction parameter. Values of L_{CuCo}, L_{FeCu}, L_{CoFe} and L_{CuCoFe} were calculated from the literature [44, 48-50]. For the later stage of aging where the coarsening of the precipitates only is taking place, C^{∞}_{Co} and C^{∞}_{Fe} can be approximated to C^{α}_{Co} and C^{α}_{Fe}, respectively. The solute concentration in the Cu matrix is negligibly small compared to that in the precipitate phase at any time, and thus we obtain ΔC_{Co}=0.7 and ΔC_{Fe}=0.3 for Cu-1.58Co-0.64Fe, ΔC_{Co}=0.5 and ΔC_{Fe}=0.5 for Cu-1.09Co-1.16Fe and ΔC_{Co}=0.3 and ΔC_{Fe}=0.7 for Cu-0.68Co-1.52Fe.

Table 4 lists the values of γ_{s}, γ_{001} and γ_{111} for sphere, cube and octahedron, calculated by Eqs. (29) to (32), together with the calculated values using experimental data for the Cu-2.15Co [19], Cu-1.58Co-0.64Fe [24] and Cu-1.93Fe alloys [20]. The values of γ_{s} for γ-Fe are in good accord with the value of $\gamma \approx 0.25$ Jm^{-2} previously reported by Matsuura et al. [14]. However the values of γ_{s} for Co are smaller than the values of γ = 0.3 to 1.0 Jm^{-2}, obtained by Oriani [15], Ardell and Nicholson [16] and Seno et al. [12]. The reason why our values of γ_{s} are smaller than the reported values has already been discussed in our previous studies [17, 19]. For each alloy $\gamma_{\mathrm{s}} > \gamma_{001}$, and for Cu-2.15Co and Cu-1.58Co-0.64Fe $\gamma_{001} \approx \gamma_{111}$. The values of γ_{s}, γ_{001} and γ_{111} increase with increase in the Fe composition of the alloys, namely Fe concentration in the Co-Fe precipitate. According to Becker [51], the energy of the coherent

interface is expressed in terms of the change in total bond energies across the interface. Thus the increase in $\gamma(\boldsymbol{n})$ with Fe composition in Co-Fe precipitates may be attributed to increase in the Cu-and-Fe bonds at the interface.

It is well known that values of K_s and $k_{s,i}$ are influenced by finite ϕ of precipitates present during coarsening in binary systems since the diffusion distance of solute atoms in the system with vanishingly small ϕ becomes longer than that in the system with finite ϕ. Numerous models to correct K_s and $k_{s,i}$ have been developed [41-43]. It would thus be inferred that the present values of K_n and $k_{n,i}$ in Tables 1 and 2 are affected by ϕ. Since the mathematical treatment of the concentration field in the GKV theory is the same as that in the LSW and KV theories for spherical particles, we can correct the values of K_n and $k_{n,i}$ in Tables 1 and 2 by the developed models. However, it is unnecessary for the calculation of $\gamma(\boldsymbol{n})$ using Eq. (29) to correct for ϕ of precipitates, because the influencing factors cancel each other, as shown by Chellman and Ardell [5].

As seen in Figs. 5 and 6, the coarsening rates of EVS precipitates show no changes with shape transitions from a sphere to a cube. Moreover, even in the cases that the precipitate shape changes from a sphere to an octahedron via a cube, we have found that the coarsening rate constants of EVS precipitates exhibit no changes [19, 24]. Since the coarsening rate of a surface element at a given temperature is dependent upon only the interface energy, as revealed in section 3, the relation $\gamma_s = g_{001}\gamma_{001} = g_{111}\gamma_{111}$ must be satisfied between the three shapes. Here g_{001} and g_{111} ($=g_n$) are the ratios of the interfacial areas of the cube and octahedron to that of EVS. Using the values of γ_{001} and γ_{111} in Table 4, and g_{001}=1.24 and g_{111}=1.18, we had the seventeen values of $g_{001}\gamma_{001}$ and $g_{111}\gamma_{111}$ for the five alloys, which are identical to the values of γ_s in Table 4. Therefore, our conclusion that the assumption (b) for the Wulff construction holds true even when the assumption (a) is not valid is justified.

From application of the KV theory to the coarsening data of spherical Co-Fe precipitates in the Cu-1.58Co-0.64Fe alloy, Watanabe et al. [24] determined the

pre-exponential factor D_0 and activation energy Q for diffusion of Co and Fe in Cu. In this study, from a similar approach using the K_n, $k_{n,\mathrm{i}}$ C^{α}_{Co} and C^{α}_{Fe} values, we have calculated values of $D_{0\mathrm{s}}$ and Q_{s} and $D_{0\mathrm{c}}$ and Q_{c} for spherical and cuboidal precipitates in the three ternary Cu-Co-Fe alloys, as summarized in Table 5. The resultant values of D_0 and Q for Co and Fe in Cu are in agreement with those obtained by tracer diffusion technique [46, 52]. In this calculation of the diffusivities, the correction for ϕ is theoretically necessary. In this study, however, the effect of ϕ on the K_n and $k_{n,\mathrm{i}}$ values is neglected because the present values of ϕ ≈ 0.018 are very small.

5. 2 Energy analysis on precipitate shape transition

Onaka et al. [53] and Satoh and Johnson [54] have shown that, in some cases of coherent precipitates in cubic materials, the precipitate shape is controlled by minimization of the sum of the elastic strain energy and interface energy of a precipitate. Moreover, Onaka et al. [36] have calculated the elastic strain energies E_{s}, E_{001} and E_{111} ($=E_n$) per unit volume of cubic materials containing spherical, {001}-cuboidal and {111}-octahedral precipitates with a purely dilatational misfit strain, using the supersphere concept. In their energy calculations, the elastic anisotropy of the Cu matrix has been brought into consideration. In the present and previous studies [17-19, 24], the spherical-to-cuboidal and cuboidal-to-octahedral shape changes with increase in size took place. We will consider the sum of the elastic strain and interface energies of a precipitate so as to analyze the shape transitions subsequently.

Assuming that the shapes of precipitates are perfect sphere, cube and octahedron, the total free energy $G_{\mathrm{t},n}$ of a precipitate can be written as [53]

$$G_{\mathrm{t},n} = 4\pi r^2 \gamma(\boldsymbol{n}) g_n + E_n 4\pi r^3 / 3 \tag{33}$$

According to Onaka et al. [36], $E_n = \Phi C_{44} \varepsilon^2$, where Φ is a shape-dependant constant, C_{44} is the shear modulus of the matrix and ε is the purely dilatational misfit strain of precipitate phase. In

the previous study [18], we obtained ε = -0.018 and -0.016 for fcc Co and γ-Fe, respectively, from length-change measurements. When a linear relation is assumed between the composition and misfit strain of a Co-Fe precipitate, we have ε=-0.0174, -0.017 and -0.0166 for Cu-1.58Co-0.64Fe, Cu-1.09Co-1.16Fe and Cu-0.68Co-1.52Fe. These values of ε, C_{44} = 7.54 x 10^{10} Pa of Cu [55], and Φ = 2.56, 2.39 and 2.67 for sphere, cube and octahedron [36] are employed to obtain values of E_n. Using the averages of γ_s, γ_{001} and γ_{111} for each alloy in Table 4, the values of g_{001}=1.24 and g_{111}=1.18, and the values of E_n, values of $G_{t,n}$ are calculated from Eq. (33) as a function of r. Fig. 10 plots $G_{t,n}$ against r for the Cu-1.58Co-0.64Fe alloy. In the rage of 0<r<7 nm, $G_{t,s}$ for sphere is smaller than $G_{t,001}$ for cube, but when r > 7 nm, this situation is reversed. This means that the spherical shape is energetically favorable when the precipitate is smaller than 7 nm in radius. This corresponds to our result that the spherical-to-cuboidal transition of Co-Fe precipitates in the alloy occurs at $r \approx 10$ nm. Similar r dependences of $G_{t,s}$ and $G_{t,001}$ were observed for Cu-2.15Co, Cu-1.09Co-1.16Fe, Cu-0.68Co-1.52Fe and Cu-1.93Fe. The calculated sizes for the spherical-to-cuboidal transitions are 7, 11, 14 and 20 nm for Cu-2.15Co, Cu-1.09Co-1.16Fe, Cu-0.68Co-1.52Fe and Cu-1.93Fe, which are in reasonable agreement with the experimentally obtained values of $r \approx 10$ [19], 15, 20 and 25 nm. It is also seen from Fig. 10 that $G_{t,111}$ for octahedron is the largest in the range of 0<r<60 nm. This is inconsistent with our result of the cuboidal-to-octahedral shape change at $r \approx 40$ nm for Cu-1.58Co-0.64Fe. For Cu-2.15Co also, $G_{t,111}$ is the largest in the range, and thus the cuboidal-to-octahedral shape change at $r \approx 30$ nm cannot be explained.

Takeda et al. [56] have reported the shape transitions of Co precipitates from a sphere to a {111}-faceted octahedron in Cu-1at%Co and Cu-3at%Co alloys aged at 873 and 1073 K by TEM observations. They have pointed out that magnetostriction plays an important role in determining the shapes of Co precipitates. In the present work also, it might be necessary for the cuboidal-to-octahedral shape change to consider the effect of magnetostriction.

6. Conclusions

(1) The theory of Ostwald ripening of spherical particles in ternary systems developed by Kuehmann and Voorhees (KV) [4] has been generalized to particles with any centro-symmetric shape. The time exponents of the average particle size, supersaturation at infinity and particle number density, being a function of the anisotropic interface energy, are identical to those found by KV.

(2) The Ostwald ripening of fcc Co-Fe precipitates in a Cu-1.01wt%Co-1.04wt%Fe and a Cu-0.63wt%Co-1.33wt%Fe alloy has been investigated by combined techniques of transmission electron microscopy observations and electrical resistivity measurements. Co-Fe precipitates smaller than 15 and 20 nm in radius in the former and the latter alloy are spherical, and larger Co-Fe precipitates have a cuboidal shape faceted on {001}. Coarsening data collected for fcc Co, Fe and Co-Fe precipitates having spherical, {001}-faceted cuboidal and {111}-faceted octahedral shapes in Cu-2wt%Co [19], Cu-1.7wt%Fe [20] and Cu-1.47wt%Co-0.56wt%Fe [24] alloys have been reexamined. The average sizes of the spherical, cuboidal and octahedral fcc precipitates increase with aging time t as $t^{1/3}$, as predicted by the generalized KV theory. The kinetics of the decay of the matrix supersaturation follow the predicted $t^{-1/3}$ law. The number densities of the spherical, cuboidal and octahedral fcc precipitates decrease with t as t^{-1}, in accordance with the prediction of the generalized KV theory.

(3) A classical thermodynamic analysis shows that usage of the generalized KV theory permits us to accurately determine the interface energy of any centro-symmetric particle even when the Wulff construction is not strictly valid in actual systems. By applying the generalized KV theory to the coarsening data of spherical, cuboidal and octahedral fcc precipitates in the Cu-Co, the three Cu-Co-Fe and the Cu-Fe alloys, the energies γ_s, γ_{001} and γ_{111} for sphere, {001}

and {111} interfaces have been determined. The estimates of γ_s, γ_{001} and γ_{111} are summarized in Table 4. Their values increase with increase in the Fe composition in the alloys.

Acknowledgements

We thank Professor K. Tazaki, Kanazawa University, for use of JEOL 2010FEF and 2000EX. A part of this work was conducted in Kyoto-Advanced Nanotechnology Network, supported by "Nanotechnology Network" of the Ministry of Education, Culture, Sports, Science and Technology (MEXT), Japan.

Appendix A. Solving method for asymptotic behavior of the average particle size, far-field supersaturation and number density

The time dependences of the average particle size $\overline{\lambda_0}$, the far-field supersaturation and the number density of particles can be determined by considering the behavior of the system in the long-time limit. Following the basic idea of Voorhees [28] and Marqusee and Ross [57], we will obtain asymptotic solutions for above three quantities.

The distribution function $f(\lambda_0, t)$ specifies the number of particles with size λ_0 per unit volume and is related to the total number $F(t)$ of particles per unit volume as

$$F(t) = \int_0^\infty f(\lambda_0, t) d\lambda_0 \qquad \text{(A1)}$$

The distribution function can change by growth of particles, by dissolution of particles and by nucleation of particles. However, we focus on the coarsening stage of particles, where the nucleation rate is negligible. In this case, the evolution of the distribution function obeys a continuity equation

$$\frac{\partial f}{\partial t} + \frac{\partial \left[\dot{\lambda}_0 f \right]}{\partial \lambda_0} = 0 \qquad \text{(A2)}$$

The volume fraction of particles ϕ is given by

$$\phi = \omega \int_0^\infty \lambda_0^3 f d\lambda_0 \tag{A3}$$

Considering the total mass, the solute concentrations in the matrix at infinity can then be expressed in terms of alloy composition $C_{i,\mathrm{a}}$ as

$$C_{i,\mathrm{a}} = C_i^\infty (1-\phi) + C_i^\beta \phi \tag{A4}$$

The system is now specified by the continuity equation (Eq. (A2)), the mass conservation constraint (Eqs. (A3) and (A4)) and the particle growth rate (Eq. (10) in the text). In order to reduce variables, we define

$$\rho_0 = \frac{\lambda_0}{L_{C2}} \tag{A5}$$

$$\tau = \frac{\eta}{3\omega} \frac{2V_\mathrm{m}}{(L_{C2})^3} \frac{\gamma_0}{\Lambda} t \tag{A6}$$

$$\frac{C_{i,\mathrm{a}} - C_i^\alpha}{C_i^\alpha} = \theta_{0,i} \tag{A7}$$

$$\frac{C_i^\infty - C_i^\alpha}{C_i^\alpha} = \theta_i^\infty \tag{A8}$$

According to the method outlined by Voorhees [28] with above reduced variables, we have Eqs. (11) to (15) in the limit $\tau \to \infty$. Here, we can change λ_0 and γ_0 to $\lambda(\boldsymbol{n})$ and $\gamma(\boldsymbol{n})$ without losing the generality since the symbols λ_0 and γ_0 are representative variables for a certain orientation.

References

[1] Lifshitz IM, Slyozov VV. J Phys Chem Solids 1961;19:35.

[2] Wagner C. Z Elektrochem 1961;65:581.

[3] Ardell AJ. Acta Metall 1967;15:1772.

[4] Kuehmann CJ, Voorhees PW. Metall Mater Trans A 1996;27A:937.

[5] Chellman DJ, Ardell AJ. Acta Metall 1974;22:577.

[6] Qiu YY. J Mater Sci 1996;31:4311.

[7] Nakayama M, Furuta A, Miura Y. Mater Trans JIM 1997;38:852.

[8] Noble B, Bray SE: Philos Mag A 1999;79:859.

[9] Marquis EA, Seidman DN: Acta Mater 2005;53:4259.

[10] Livingston JD. Trans Met Soc AIME 1959;215:566.

[11] Phillips VA. Philos Mag 1965;11:775.

[12] Seno Y, Tomokiyo Y, Oki K, Eguchi T. Trans JIM 1983;24:491.

[13] Amin K, Gerold V, Kralik G. J Mater Sci 1975; 10:1519.

[14] Matsuura K, Kitamura K, Watanabe K. J Jpn Inst Metals 1977;41:1285.

[15] Oriani RA. Acta Metall 1964;12:1399.

[16] Ardell AJ, Nicholson RB. J Phys Chem Solids 1966;27:1793.

[17] Watanabe D, Higashi K, Watanabe C, Monzen R. J Jpn Inst Metals 2007;71:151.

[18] Watanabe D, Watanabe C, Monzen R. J Mater Sci 2008; 43: 3946.

[19] Watanabe D, Watanabe C, Monzen R. Metall Mater Trans A 2008; 39A: 725.

[20] Monzen R, Kita K. Philos Mag Lett 2002;82:373.

[21] Lin M, Olson GB, Cohen M. Acta Metall Mater 1993;41:253.

[22] Monzen R, Kato M, Mori T. Acta Metall 1989;37:3177.

[23] Monzen R, Kato M. J Mater Sci Lett 1992;11:56.

[24] Watanabe C, Watanabe D, Monzen R. J Mater Sci 2008; 43: 3817.

[25] Wulff G. Zeit f Kryst 1901;34:449.

[26] Johnson CA. Surf Sci 1965;3:429.

[27] Sutton AP, Balluffi RW. Interfaces in Crystalline Materials. Oxford: Clarendon Press; 1995.

[28] Voorhees PW. Metall Trans A 1990;21A:27.

[29] Wimmel J, Ardell AJ. Mater Sci Eng A 1994;A183:169.

[30] Onaka S, Kobayashi N, Fujii T, Kato M. Mater Sci Eng A 2003;A347:42.

[31] Johnson WC. Acta Metall 1984;32:465.

[32] Johnson WC, Voorhees PW, Zupon DE. Metall Trans A 1989;20A:1175.

[33] Dehoff R. Thermodynamics in Materials Science. 2nd ed. Boca Raton: CRC Press; 2006.

[34] Eshelby JD. Proc R Soc 1957;A241:376.

[35] Mura T. Micromechanics of defects in solids. Dordrecht: Martinus Nijhoff; 1987.

[36] Onaka S, Fujii T, Kato M. Acta Mater 2007;55:669.

[37] Linde JO. Helv Phys Acta 1968;41:1007.

[38] Kato M, Monzen R, Mori T. Acta Metall 1978;26:605.

[39] Ardell AJ. Philos Mag 1967;16:147.

[40] Fujii T, Tamura T, Kato M, Onaka S. Microsc Microanal 2002;8:1434.

[41] Ardell AJ. Acta Metall 1972;20:61.

[42] Voorhees PW, Glicksman ME. Metall Trans A 1984;15A:1081.

[43] Wang KG, Glicksman ME, Rajan K. Comput Mater Sci 2005;34:235.

[44] Wang CP, Liu XJ, Ohnuma I, Kainuma R, Ishida K. J Phase Equilib 2002;23:236.

[45] Ardell AJ. Mater Sci Eng A 1997;A238:108.

[46] Dohl R, Macht MP, Naundorf V. Phys Status Solidi A 1984;86:603.

[47] Heinrich B, Cochran JF, Kowalewski M, Kirschner J, Celinski Z, Arrott AS, Myrtle K. Phys Rev B 1991;44:9348.

[48] Ohnuma I, Enoki H, Ikeda O, Kainuma R, Ohtani H, Sundman B, Ishida K. Acta Mater 2002;50:379.

[49] Palumbo M, Stefano C, Battezzati L. Calphad 2006;30:171.

[50] Turchanin MA, Agraval PG, Nikolaenko IV. J phase Equilib 2003;24:307.

[51] Becker R. Ann Physik, 1938;32:128.

[52] Japan Institute of Metals. Kinzoku data book. Tokyo: Maruzen; 2004. p. 37.

[53] Onaka S, Kobayashi N, Fujii T, Kato M. Intermetallics 2002;10:343.

[54] Satoh S, Johnson WC. Metall Trans A 1992;23A:2761.

[55] Overton Jr WC, Caffney J. Phys Rev 1955;98:969.

[56] Takeda M, Suzuki N, Shinohara G, Endo T, Landuyt JV. Phys Status Solidi A 1998;168:27.

[57] Marqusee JA, Ross J. J Chem Phys 1983;79:373.

Figure and Table captions

Fig. 1 Definition of the geometric parameters of a particle with 3-dimensionally-point symmetric shape.

Fig. 2 Results of EDX analysis obtained from Co-Fe precipitates in a Cu-0.68at%Co-1.52at%Fe alloy aged at 973 K for 10 min and 48 h. The ordinate and abscissa are shown in atomic fraction.

Fig. 3 Bright-field images of Co-Fe precipitates in a Cu-0.68at%Co-1.52at%Fe alloy aged at 973 K for (a) 30 min and (b) 48 h. The zone axis is [001].

Fig. 4 Bright-filed images of Co-Fe precipitates in a Cu-1.09at%Co-1.16at%Fe alloy aged at 973 K for (a) 30 min and (b) 48 h. The inset at the upper right in (a) is a magnified dark-field image of a bcc Co-Fe precipitate. The zone axis is [001].

Fig. 5 Variation in the average sizes $\overline{\lambda}(\boldsymbol{n})$ of spherical (S) and cuboidal (C) precipitates with aging time t for (a) Cu-0.68at%Co-1.52at%Fe and (b) Cu-1.09at%Co-1.16at%Fe alloys aged at 873, 923 and 973 K. For cuboidal precipitates, radii of equivalent-volume sphere (EVS) are also shown. Lines with slope of 1/3 are superimposed.

Fig. 6 Coarsening plots of spherical (S) and cuboidal (C) Co-Fe precipitates in a Cu-0.68at%Co-1.52at%Fe alloy aged at 873, 923 and 973 K. For cuboidal precipitates, data for equivalent-volume sphere (EVS) are also shown.

Fig. 7 Size distributions of Co-Fe precipitates in a Cu-0.68at%Co-1.52at%Fe alloy aged at 973 K for (a) 30 min, (b) 48 h, in a Cu-1.09at%Co-1.16at%Fe alloy aged at 973 K for (c) 30 min, (d) 48 h, and in a Cu-1.58at%Co-0.64at%Fe alloy aged at 973 K for (e) 30 min, (f) 32.5 h and (g) 334 h. The size distribution predicted by the LSW theory is superimposed on each histogram. The number of precipitates measured, the average precipitate size $\bar{\lambda}(\boldsymbol{n})$ and the precipitate shape are also shown.

Fig. 8 Variation in the far-filed concentrations C_{Co}^{∞} and C_{Fe}^{∞} of Co and Fe in the matrix of a Cu-0.68at%Co-1.52at%Fe alloy aged at 873, 923 and 973 K as a function of $t^{-1/3}$.

Fig. 9 Variation in the number density F of spherical (S) and cuboidal (C) precipitates with aging time t for a Cu-0.68at%Co-1.52at%Fe alloy aged at 873, 923 and 973 K. The dotted triangle indicates the slope of -1 predicted from Eq. (15). The values calculated from Eq. (28) are represented by straight lines.

Fig. 10 Plots of the sum $G_{\mathrm{t},n}$ of the interface energy and elastic strain energy, calculated from Eq. (33), of spherical, cuboidal and octahedral precipitates in a Cu-1.58at%Co-0.64at%Fe alloy as a function of radius r of equivalent-volume sphere.

Table 1 Rate constants K_{s} and K_{001} for spherical and cuboidal precipitates in Cu-1.09at%Co-1.16at%Fe and Cu-0.68at%Co-1.52at%Fe alloys. Also shown are values of K_{s}, K_{001} and K_{111} for octahedral precipitates, calculated using coarsening data for Cu-2.15at%Co [19], Cu-1.58at%Co-0.64at%Fe [24] and Cu-1.93at%Fe [20] alloys.

Table 2 Coarsening parameters $k_{n,\mathrm{Co}}$ and $k_{n,\mathrm{Fe}}$ for Cu-1.09at%Co-1.16at%Fe and Cu-0.68at%Co-1.52at%Fe alloys containing spherical and cuboidal precipitates. Also shown are values of $k_{n,\mathrm{Co}}$ and $k_{n,\mathrm{Fe}}$ for Cu-2.15at%Co [19], Cu-1.58at%Co-0.64at%Fe [24] and Cu-1.93at%Fe [20] alloys containing spherical, cuboidal and octahedral precipitates.

Table 3 Equilibrium concentrations C_{Co}^{α} and C_{Fe}^{α} of Co and Fe in the Cu matrix of Cu-1.09at%Co-1.16at%Fe and Cu-0.68at%Co-1.52at%Fe alloys, obtained from analysis of data on coarsening. The concentration is expressed in atomic fraction. Also shown are reported values of C_{Co}^{α} and C_{Fe}^{α} for Cu-1.08at%Co [17], Cu-1.58at%Co-0.64at% Fe [24] and Cu-1.93at%Fe [20] alloys.

Table 4 Energies γ_{s} and γ_{001} of sphere and {001} interfaces of Co-Fe precipitates in Cu-1.09at%Co-1.16at%Fe and Cu-0.68at%Co-1.52at%Fe alloys, obtained using Eq. (29). Also shown are values of γ_{s}, γ_{001} and γ_{111} for {111} interface of precipitates, calculated using data for Cu-2.15at%Co [19], Cu-1.58at%Co-0.64at%Fe [24] and Cu-1.93at%Fe [20] alloys.

Table 5 Pre-exponential factors $D_{0\mathrm{s}}$ and $D_{0\mathrm{c}}$ and activation energies Q_{s} and Q_{c} for diffusion of Co and Fe in Cu, estimated using data on coarsening of spherical and cuboidal precipitates in Cu-1.09at%Co-1.16at%Fe and Cu-0.68at%Co-1.52at%Fe alloys. Also shown are values calculated using coarsening data for a Cu-1.58at%Co-0.64at%Fe [24] alloy, and values of D_0 and Q for impurity diffusion of Co [46] and Fe [52] in Cu obtained by tracer diffusion technique.

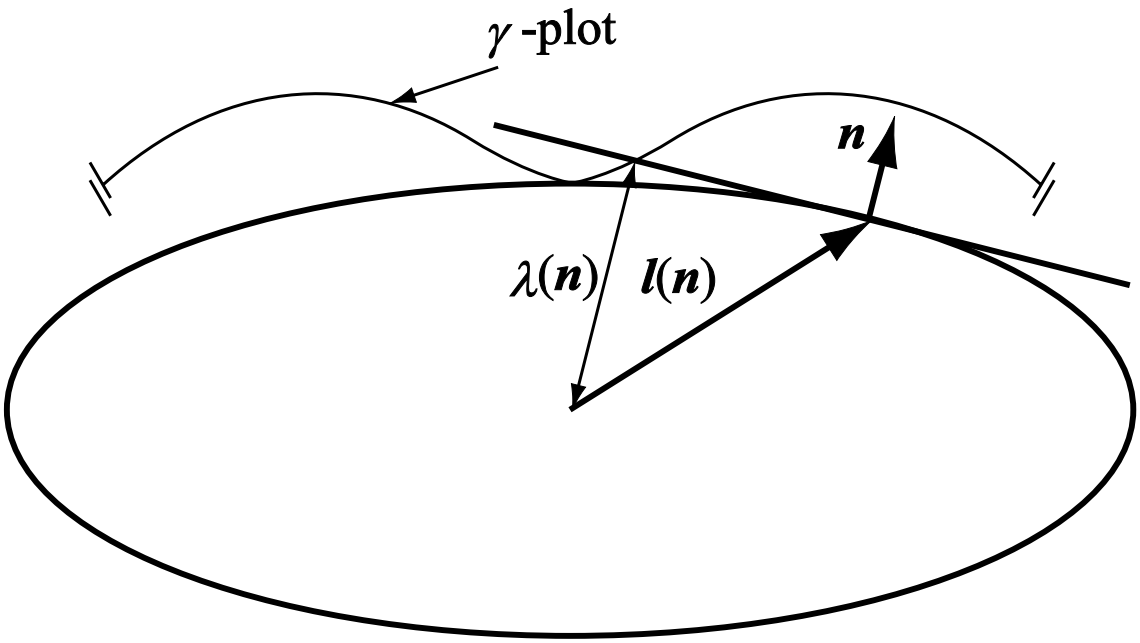
γ -plot
n
λ(n)
l(n)

Fig. 1

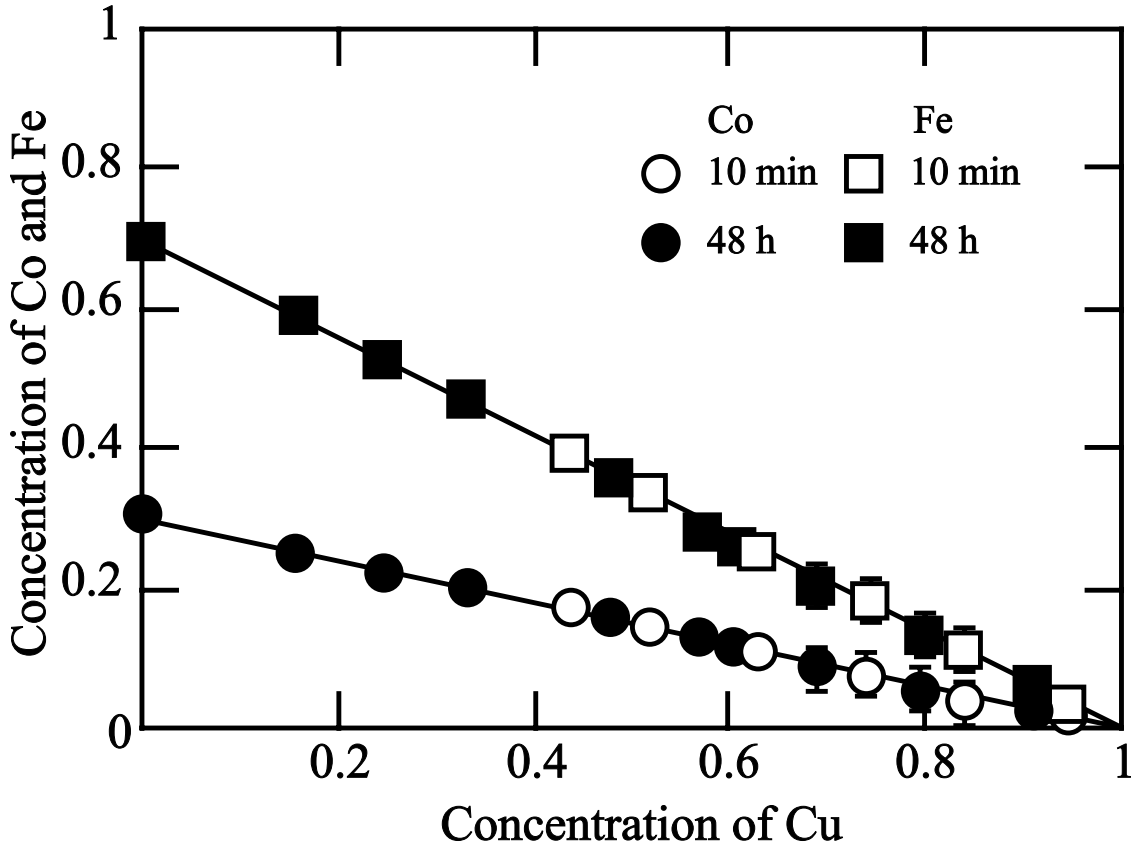
Co
Fe
10 min
10 min
48 h
48 h
Concentration of Co and Fe
Concentration of Cu
0
0.2
0.4
0.6
0.8
1

Fig. 2

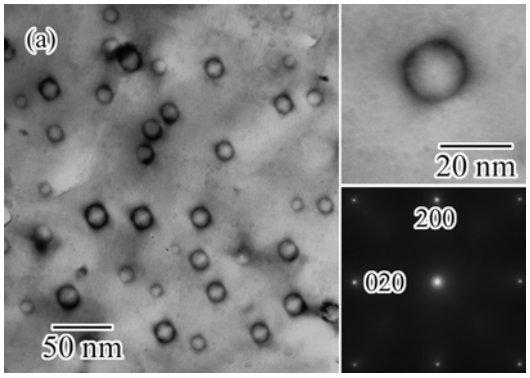
(a)
20 nm
200
020
50 nm

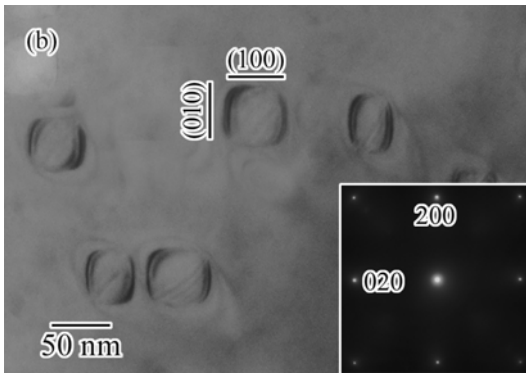
(b)
(100)
(010)
200
020
50 nm

Fig. 3

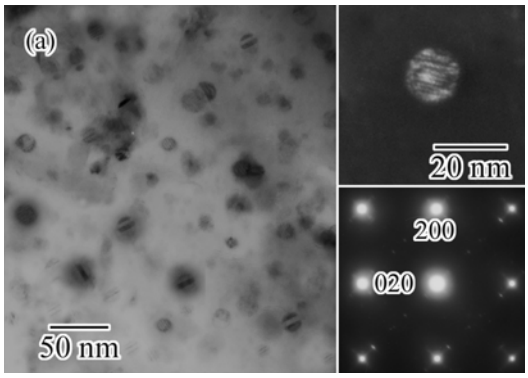
(a)
20 nm
200
020
50 nm

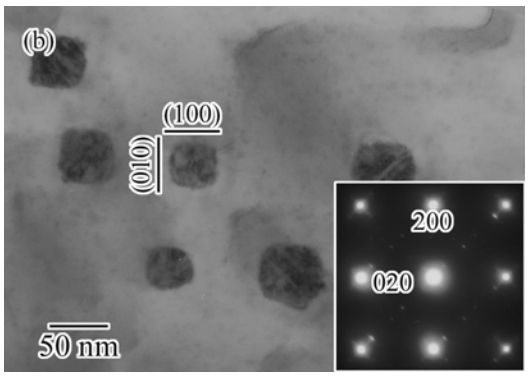
(b)
(100)
(010)
200
020
50 nm

Fig. 4

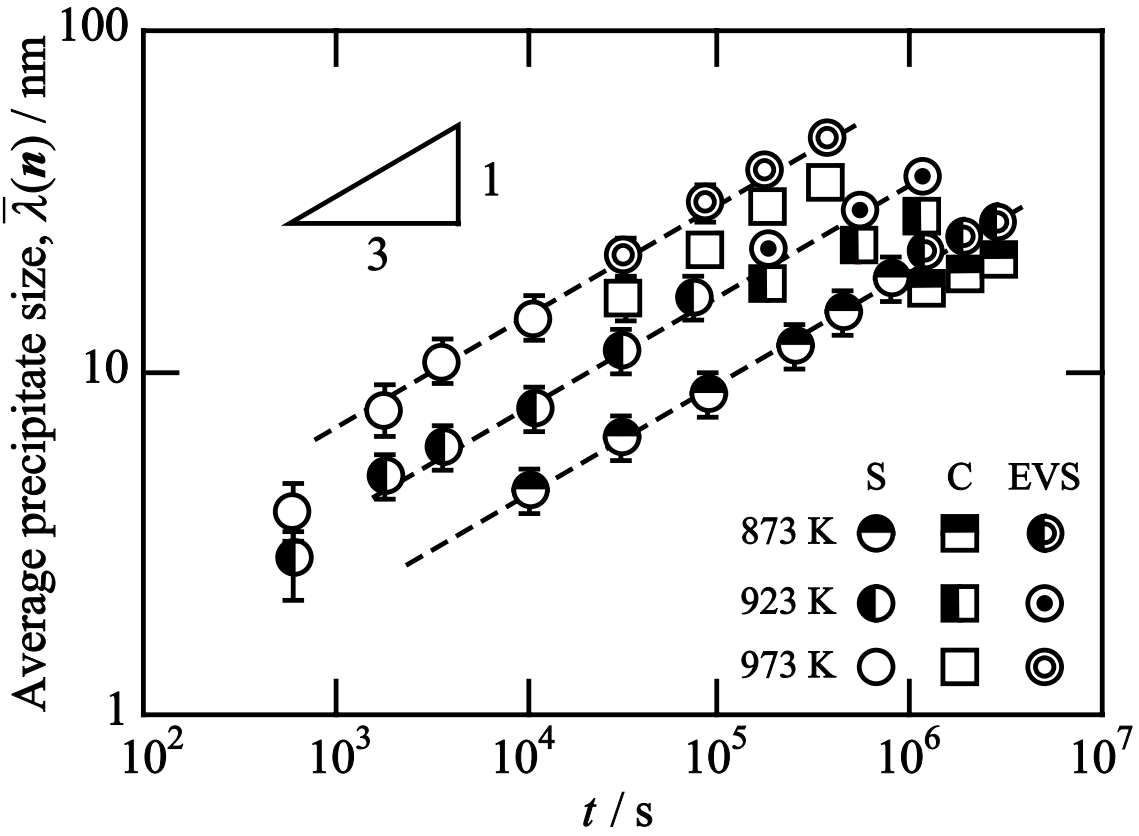
100
10
1
Average precipitate size, $\bar{\lambda}(n)$ / nm
1
3
S
C
EVS
873 K
923 K
973 K
10^2
10^3
10^4
10^5
10^6
10^7
t / s

Fig. 5(a)

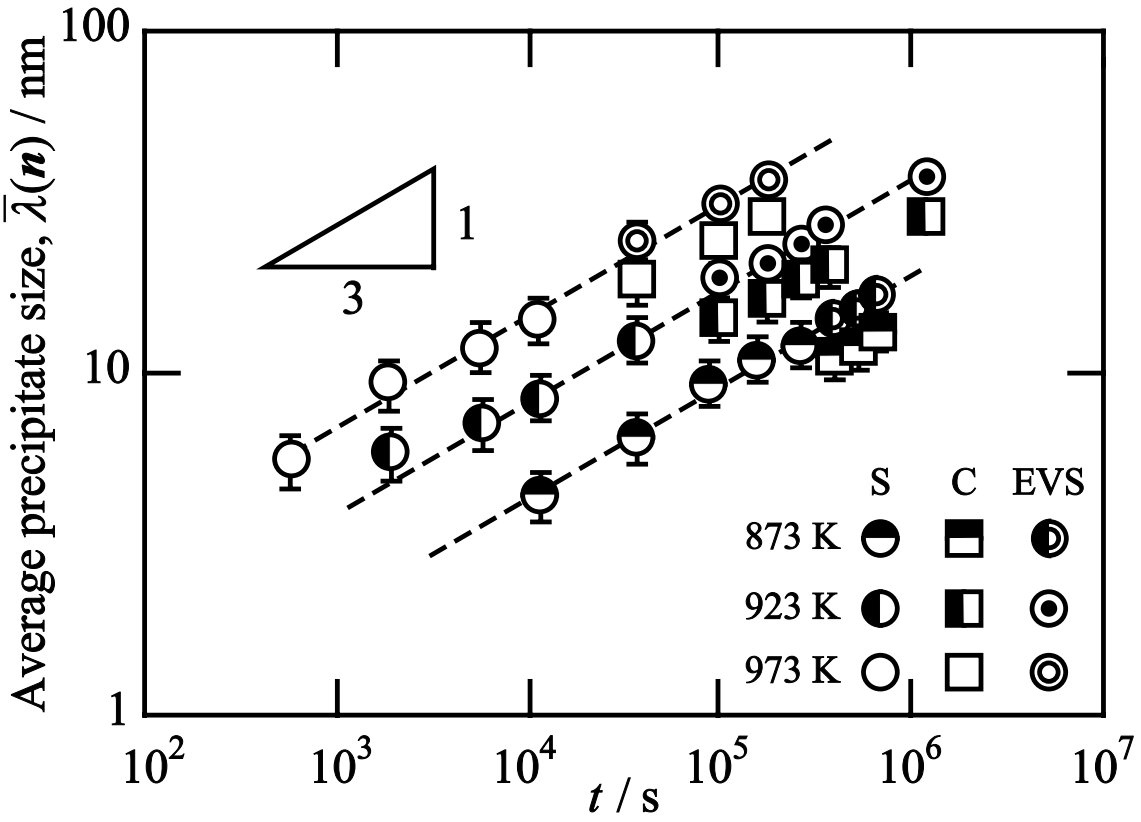
100
10
1
Average precipitate size, $\bar{\lambda}(n)$ / nm
1
3
S
C
EVS
873 K
923 K
973 K
10^2
10^3
10^4
10^5
10^6
10^7
t / s

Fig. 5(b)

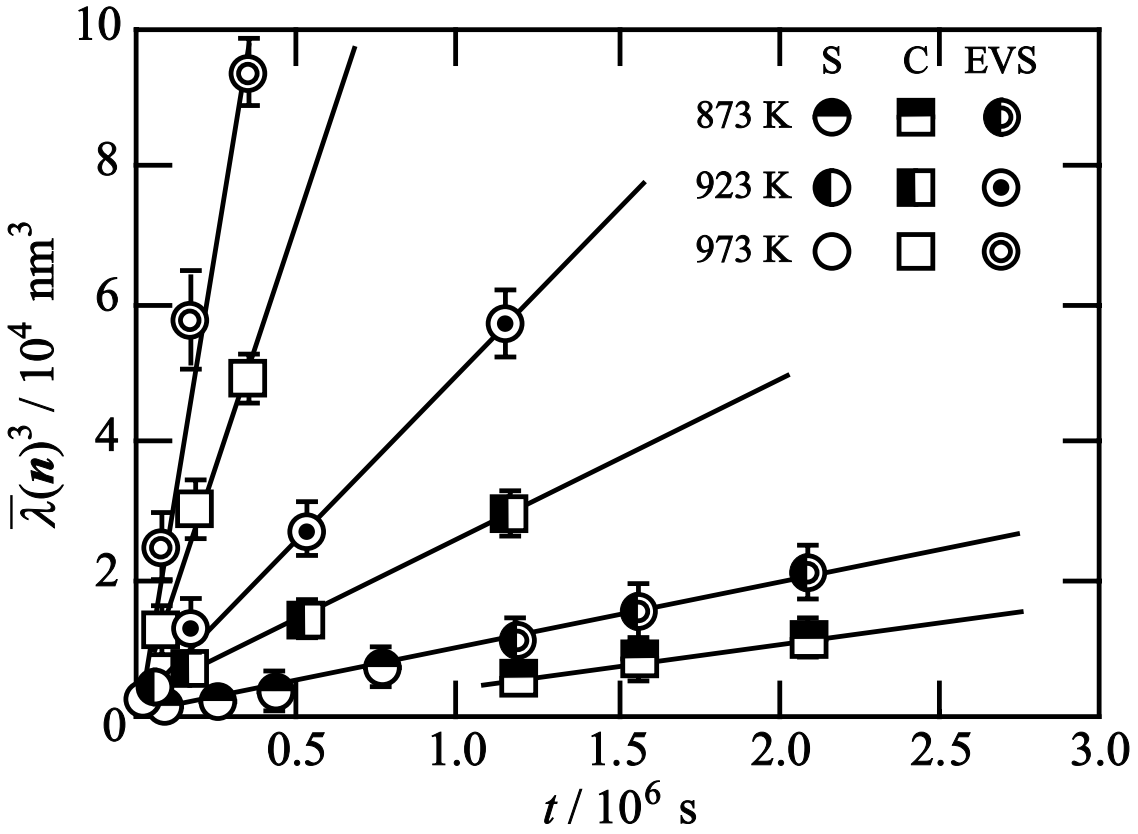
S
C
EVS
873 K
923 K
973 K
$\overline{\lambda(n)}^3 / 10^4$ nm^3
$t / 10^6$ s
0
2
4
6
8
10
0.5
1.0
1.5
2.0
2.5
3.0

Fig. 6

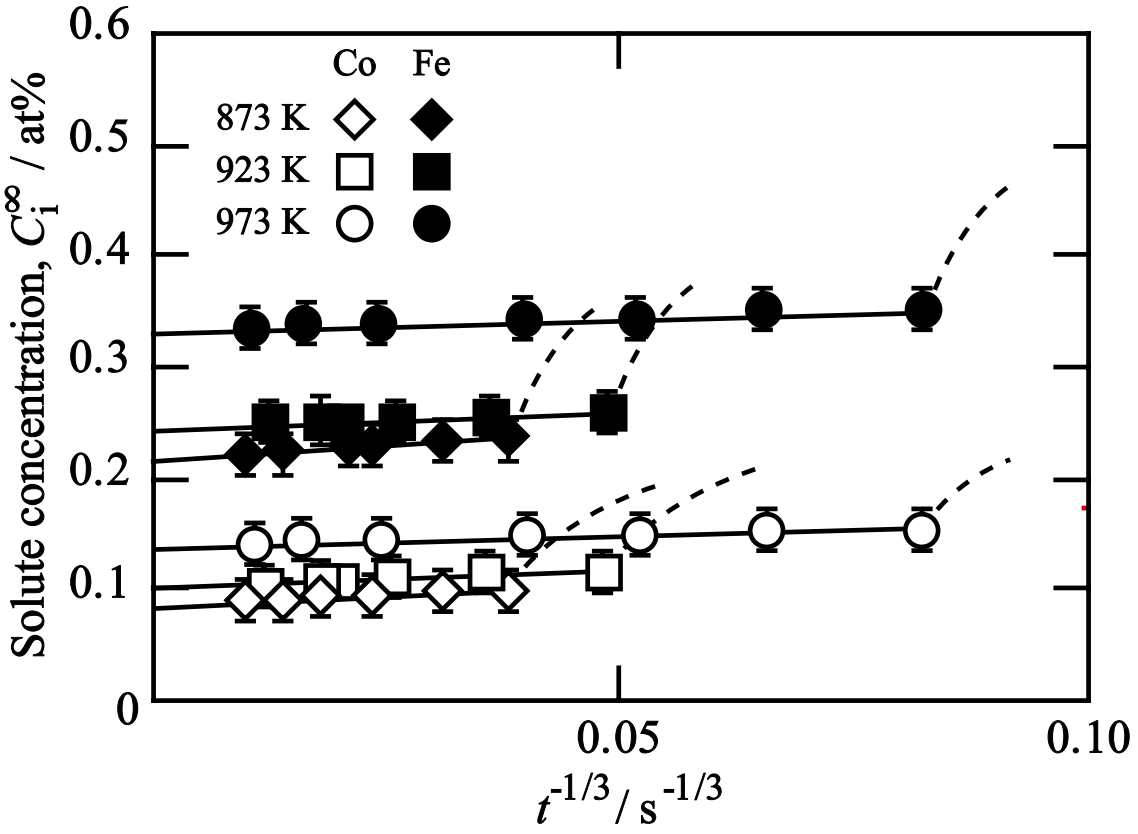
Co Fe
873 K
923 K
973 K
Solute concentration, C_i^∞ / at%
0.6
0.5
0.4
0.3
0.2
0.1
0
0.05
0.10
$t^{-1/3}$ / $s^{-1/3}$

Fig. 7

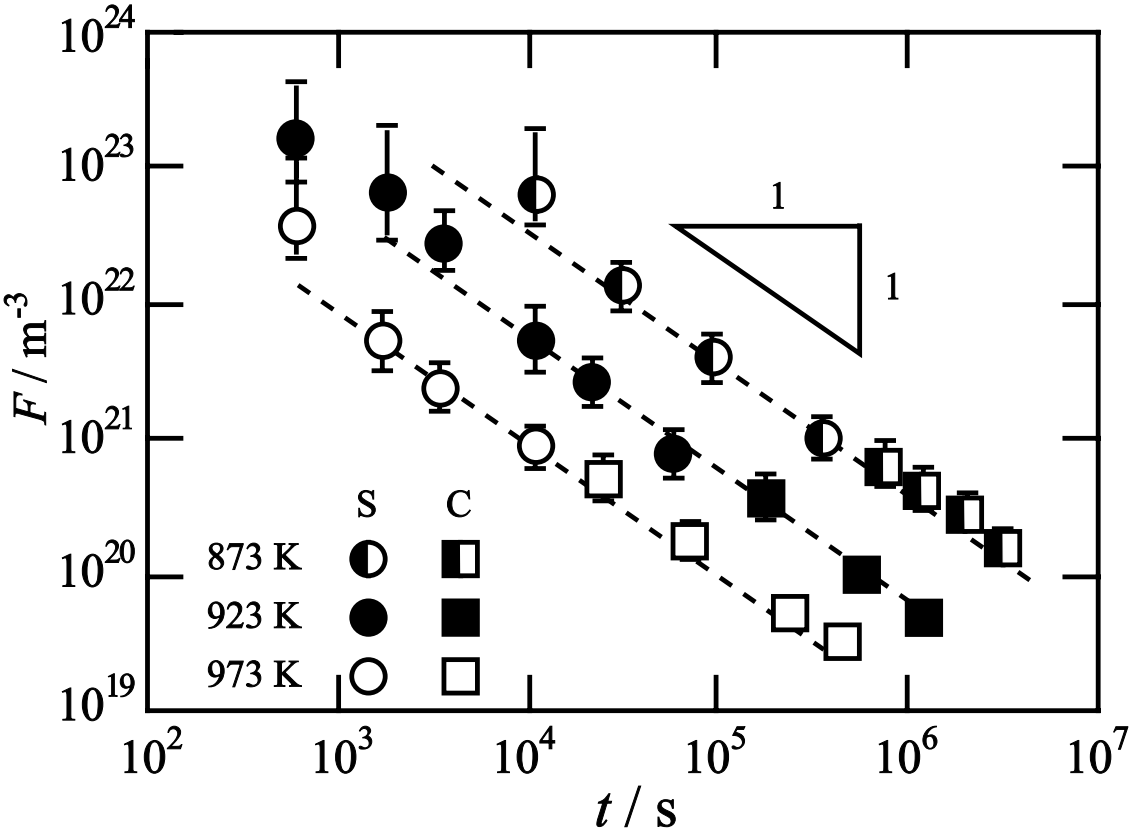
10^{24}
10^{23}
10^{22}
10^{21}
10^{20}
10^{19}
F / m^{-3}
1
1
S
C
873 K
923 K
973 K
10^2
10^3
10^4
10^5
10^6
10^7
t / s

Fig. 8

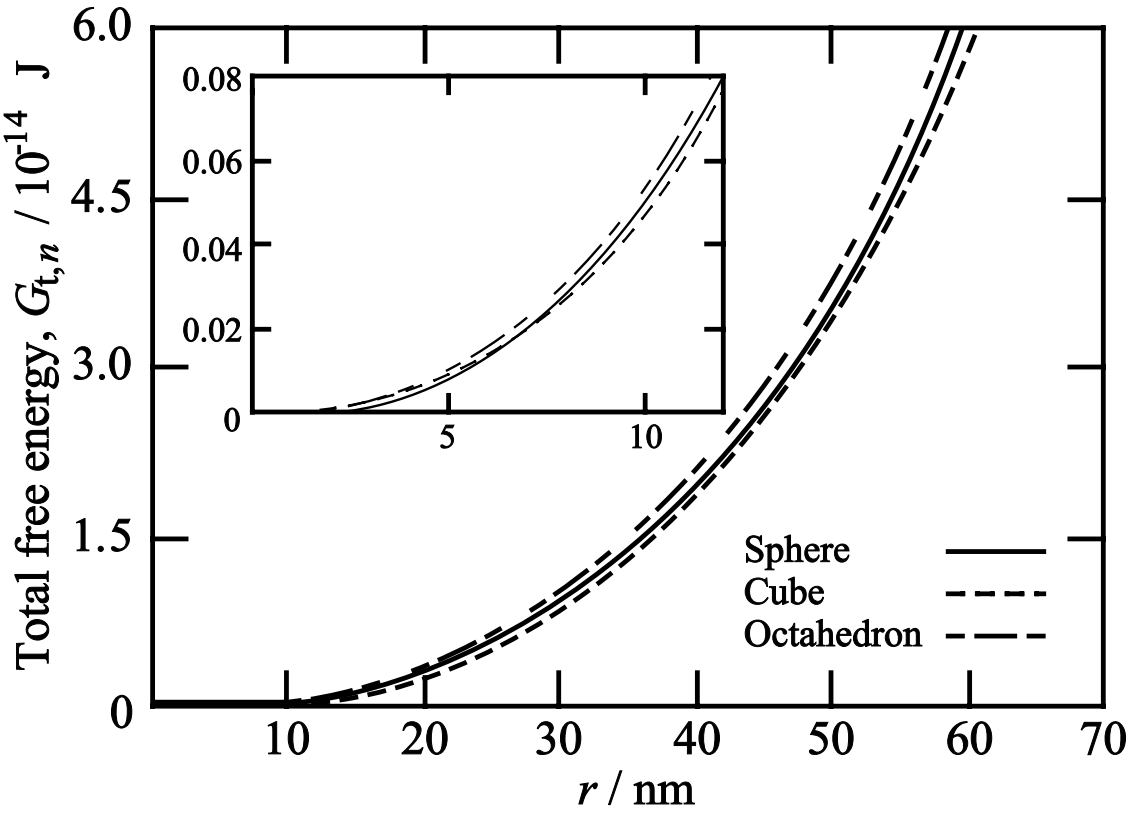
Total free energy, $G_{t,n}$ / 10^{-14} J
6.0
4.5
3.0
1.5
0
10
20
30
40
50
60
70
r / nm
0.08
0.06
0.04
0.02
0
5
10
Sphere
Cube
Octahedron

Fig. 9

Table 1

T (K)	K_s (10^{-30} m^3 s^{-1})					K_{001} (10^{-30} m^3 s^{-1})					K_{111} (10^{-30} m^3 s^{-1})	
	Cu–2.15Co[12]	Cu–1.58Co –0.64Fe[17]	Cu–1.09Co –1.16Fe	Cu–0.68Co –1.52Fe	Cu–1.93Fe[13]	Cu–2.15Co	Cu–1.58Co –0.64Fe	Cu–1.09Co –1.16Fe	Cu–0.68Co –1.52Fe	Cu–1.93Fe	Cu–2.15Co	Cu–1.58Co –0.64Fe
873	5.80	8.80	8.30 ± 0.9	9.00 ± 0.7	6.44	3.04	4.82	4.75 ± 0.4	5.30 ± 0.4	3.37	–	–
923	31.5	45.0	43.0 ± 3.7	47.0 ± 4.1	60.1	16.5	23.1	24.8 ± 2.2	29.0 ± 3.0	31.5	–	–
973	109	263	255 ± 28	255 ± 30	379	57.1	135	155 ± 17	170 ± 18	198	65.9	169

Table 2

T (K)	$k_{n,\mathrm{Co}}$ (10^{-3} s^{-1})				$k_{n,\mathrm{Fe}}$ (10^{-3} s^{-1})			
	Cu–2.15Co[12]	Cu–1.58Co –0.64Fe[17]	Cu–1.09Co –1.16Fe	Cu–0.68Co –1.52Fe	Cu–1.58Co –0.64Fe[17]	Cu–1.09Co –1.16Fe	Cu–0.68Co –1.52Fe	Cu–1.93Fe[13]
873	7.74	4.78	3.05 ± 0.3	1.50 ± 0.3	2.05	3.05 ± 0.3	3.50 ± 0.5	4.32
923	5.18	3.02	1.80 ± 0.1	1.10 ± 0.2	1.29	1.80 ± 0.1	2.60 ± 0.3	3.93
973	3.39	2.19	1.50 ± 0.3	0.70 ± 0.1	0.94	1.50 ± 0.3	1.63 ± 0.2	3.13

Table 3

T (K)	C^{α}_{Co} (10^{-3})				C^{α}_{Fe} (10^{-3})			
	Cu–1.08Co[10]	Cu–1.58Co –0.64Fe[17]	Cu–1.09Co –1.16Fe	Cu–0.68Co –1.52Fe	Cu–1.58Co –0.64Fe[17]	Cu–1.09Co –1.16Fe	Cu–0.68Co –1.52Fe	Cu–1.93Fe[13]
873	4.79	2.50	1.47 ± 0.001	0.68 ± 0.004	1.07	1.47 ± 0.001	1.59 ± 0.01	1.63
923	5.73	2.89	1.60 ± 0.001	0.97 ± 0.004	1.24	1.60 ± 0.001	2.26 ± 0.01	3.06
973	6.45	3.88	2.60 ± 0.001	1.17 ± 0.004	1.66	2.60 ± 0.001	2.73 ± 0.01	5.44

Table 4

T (K)	γ_s (Jm^{-2})					γ_{001} (Jm^{-2})					γ_{111} (Jm^{-2})	
	Cu–2.15Co[12]	Cu–1.58Co –0.64Fe[17]	Cu–1.09Co –1.16Fe	Cu–0.68Co –1.52Fe	Cu–1.93Fe[13]	Cu–2.15Co	Cu–1.58Co –0.64Fe	Cu–1.09Co –1.16Fe	Cu–0.68Co –1.52Fe	Cu–1.93Fe	Cu–2.15Co	Cu–1.58Co –0.64Fe
873	0.15	0.20	0.22 ± 0.03	0.24 ± 0.04	0.26	0.12	0.17	0.18 ± 0.03	0.20 ± 0.03	0.21	–	–
923	0.15	0.20	0.22 ± 0.01	0.23 ± 0.04	0.27	0.12	0.16	0.18 ± 0.02	0.19 ± 0.02	0.22	–	–
973	0.14	0.20	0.21 ± 0.04	0.22 ± 0.03	0.23	0.12	0.16	0.18 ± 0.03	0.19 ± 0.02	0.19	0.12	0.18

Table 5

	D_{0s} (10^{-5} m^{2}s^{-1})		Q_s (Jmol^{-1})		D_{0c} (10^{-5} m^{2}s^{-1})		Q_c (Jmol^{-1})	
	Co	Fe	Co	Fe	Co	Fe	Co	Fe
Cu–1.58Co–0.64Fe[17]	9.9 ± 7	17 ± 14	216 ± 8	218 ± 8	3.6 ± 3	1.9 ± 1	212 ± 10	210 ± 8
Cu–1.09Co–1.16Fe	5.1 ± 3	5.3 ± 10	210 ± 7	209 ± 9	5.1 ± 4	6.1 ± 4	214 ± 8	215 ± 10
Cu–0.68Co–1.52Fe	3.6 ± 2	6.5 ± 5	205 ± 11	209 ± 10	13 ± 11	14 ± 10	220 ± 12	218 ± 10

	D_0 (10^{-5} m^{2}s^{-1})	Q (Jmol^{-1})
Impurity diffusion of Co[33]	8.4	214
Impurity diffusion of Fe[34]	10	213